PAPER

Check for updates

Selective polyethylene hydrocracking to liquid and gaseous hydrocarbons over Co−Ni catalysts supported on H-BEA zeolite

Mahdokht Soltani, [ID] [a] Julia N. Hancock, [ID] [a] Zeno R. Ramadhan, [ID] [b]
Samuel Somerville, [ID] [b] Jamie Clark, [a] Richard Tilley [ID] [b] and Julie E. Rorrer [ID] *[a]

The global plastic waste crisis demands efficient catalytic solutions to convert polyolefins into valuable fuels and chemicals. While noble metal catalysts have shown high activity for hydrogenolysis, their high cost and scarcity hinder large-scale implementation. Hydrocracking over earth abundant acid catalysts such as zeolites remains limited by catalyst deactivation, poor selectivity, and sensitivity to moisture and contaminants. In this study, a series of cobalt−nickel bimetallic catalysts supported on H-BEA zeolite (Co−Ni/BEA) were designed to address these challenges. A Co−Ni/BEA catalyst with approximately a 1 : 1 ratio of Co : Ni, prepared *via* co-impregnation, outperformed monometallic and physical mixture analogues during hydrocracking at 265 °C and 20 bar H_2, achieving high liquid alkane yields while suppressing methane formation. Temperature- and pressure-dependent studies of model polyethylene (tetracosane) hydrocracking, in combination with a suite of catalyst characterization techniques, suggest that Co improves activity, while Ni incorporation modulates the hydrogenolysis pathway, reducing terminal C−C cleavage and improving hydrogen utilization *via* spillover. In the presence of water, Co−Ni/BEA retained high activity and low coke formation, while metal-free H-BEA produced carbonaceous deposits which clog pore sites, emphasizing the necessity of metal sites for water-tolerant upcycling. The Co−Ni/BEA catalyst selectively formed $C_3−C_7$ hydrocarbons from LDPE, demonstrating the use of earth-abundant, inexpensive transition metals as a sustainable alternative to noble metals. These findings establish a scalable, selective, and water-tolerant catalyst platform for polyethylene waste valorization.

Green foundation

1. This work pioneers earth-abundant Co–Ni/BEA catalysts for polyethylene hydrocracking, offering a selective, water-tolerant, and methane-suppressing alternative to noble metals. By coupling metal–acid bifunctionality with Co–Ni synergy, it addresses three key barriers in plastic upcycling: cost, scalability, and deactivation.

2. The optimized 1 : 1 Co : Ni catalyst achieves near complete conversion of polyethylene to liquid and gaseous alkanes ($C_3–C_{24}$) under mild conditions (265 °C, 20 bar H_2, 3 h). Unlike Co-only catalysts, which release increasing methane at elevated temperature, the bimetallic system fully suppresses methane across 265–285 °C while resisting coke formation. Importantly, partial replacement of Co with Ni reduces reliance on cobalt without compromising performance.

3. Future directions will involve reducing cobalt reliance by designing more highly dispersed bimetallic nanoparticles and exploiting pore confinement to further tune activity and selectivity. By targeting the creation of monomers, ongoing efforts will work towards a circular plastic economy.

1. Introduction

Waste plastics continue to threaten global environmental health and safety due to their poor end-of-life management and environmental persistence. In 2017, global plastic pro-duction reached 348 million tonnes, with projections indicating a fourfold increase by 2050.[1] Less than 7% of total plastic waste in the United States is recycled, with the majority accumulating in landfills (about 34 million tons in 2021), or leaking into the environment (estimated 25 million tonnes annually), posing risks to ecosystems and public health.[1–4]

Among plastics, polyolefins (POs), including low-density polyethylene (LDPE) and polypropylene (PP), are the most widely produced.[5] While mechanical recycling offers a second life to waste polyolefins, the materials tend to degrade during

[a] Department of Chemical Engineering, University of Washington 3781 Okanogan Lane, Seattle, WA 98195-1750, USA. E-mail: jrorrer@uw.edu
[b] University of New South Wales, Sydney, NSW 2052, Australia

reprocessing, often leading to contaminated or lower-quality products.[6–11] These challenges have spurred interest in chemical depolymerization strategies to convert waste into high-value fuels, chemicals, and monomers for re-manufacturing of virgin-quality plastics. Pyrolysis offers the opportunity to generate fuel-range hydrocarbons; however, this endothermic process typically requires high temperatures (up to 900 °C) and offers low product selectivity.[6,8,12–14] Hydrogenolysis has emerged as a promising method for plastic upcycling at lower operating temperatures (200–300 °C) and pressures ranging from 20–80 bar.[11] Noble metals such as Pt and Ru are highly active for hydrogenolysis but are limited by cost and scarcity.[15,18–23] Furthermore, while catalysts comprised of Ru are active at lower temperatures (200–225 °C), they tend to promote extensive C–C bond cleavage, favoring methane formation and reducing the yield of liquid-range products.[15,19,24] While increasing the hydrogen pressure has been shown to decrease methane production, the formation of methane still persists.[19]

To address these issues, earth-abundant metals (EAMs) such as cobalt and nickel have gained attention as cost-effective and scalable alternatives.[16,17,25–29] Vance et al. demonstrated that Ni/SiO$_2$ (15 wt% Ni) could selectively depolymerize LDPE into liquid-range hydrocarbons (C$_6$–C$_{35}$) at 300 °C, 30 bar H$_2$, over 12 h,[16] and more recently reported that Ni/BEA achieved up to 80% naphtha-range yields at 250 °C and 60 bar H$_2$, with productivities 2.5–6.2 times higher than prior Pt- and EAM-based systems, although performance declined sharply at lower hydrogen pressures (15 bar).[25] Tan et al. evaluated Ni/MFI (1 wt% Ni) for polyethylene hydrocracking at 200 °C and 10 bar H$_2$, achieving ~14% solid conversion with C$_3$–C$_7$ hydrocarbons as the dominant products, compared to 22% for Pt/MFI under identical conditions.[26] Borkar et al. applied Co/SiO$_2$ (5 wt% Co) for LDPE hydrogenolysis at 275 °C, 30 bar H$_2$, over 8 h, and achieved C$_5$–C$_{30}$ yields of 55% (C-mole basis).[17] However, higher Co loadings or bulk Co$_3$O$_4$ favor terminal scission, increasing CH$_4$ formation and reducing liquid selectivity.[17] Despite these advancements, monometallic EAMs still require relatively harsh conditions (250–650 °C, 10–80 bar H$_2$, 1–20 h) and typically produce less than 80% of desired C$_6$–C$_{35}$ products.[16,17,25,28,30,31]

To improve activity and selectivity, bimetallic systems have been explored due to their ability to enhance metal dispersion and promote synergistic effects.[27,29,32,33] However, many of these systems still rely on noble metals.[32,34] Although mechanistically different from hydrogenolysis, the Fischer–Tropsch synthesis (FTS) reaction also targets liquid hydrocarbons and benefits from improved hydrogen activation. As such, insights from FTS literature offer valuable context. For example, Wang et al. showed that Ni–Co/HZSM-5 catalysts improved iso-paraffin yields compared to monometallic Co, attributed to better metal dispersion.[35] Hernández Mejía et al. further demonstrated that incorporating Ni into Co-based catalysts lowered reduction temperatures, likely due to co-reduction.[36] Prior studies also suggest that such bimetallic combinations may lead to alloy formation, further improving catalytic performance.[27,37] In the context of polyolefin hydrogenolysis, Cong et al. reported that Fe-promoted

Ni/Al$_2$O$_3$ achieved liquid yields up to 79%, with 74% C$_8$–C$_{16}$ at 300 °C and 30 bar H$_2$, and attributed the improved yields to promotion of internal C–C bond scission, and suppression of methane formation via increased Ni^{2+} character, which moderates H$_2$ coverage.[27] These findings suggest that secondary metal addition can regulate hydrogen coverage and direct C–C scission pathways. By analogy, we hypothesize that such interactions in Co–Ni systems could enhance reducibility and hydrogenation efficiency in polyolefin hydrogenolysis. We further posit that supporting these metals on an acidic support will promote bifunctional hydrocracking.

The incorporation of Brønsted acid sites shifts the reaction mechanism from monofunctional hydrogenolysis, driven solely by metal-catalyzed C–C bond cleavage, to bifunctional hydrocracking, where metal sites facilitate hydrogenation/dehydrogenation steps and acid sites promote β-scission.[38,39] In this context, acidic zeolites not only promote C–C bond cleavage through Brønsted acidity but may also induce shape-selectivity effects as well.[21,40] Lee et al. systematically benchmarked Co-, Ni-, and Ru-modified silica–alumina catalysts and showed that Ni/ZSM-5 and Co/ZSM-5 produce saturated liquid and gaseous alkanes via a bifunctional hydrocracking pathway, whereas under the same conditions (45 bar H$_2$, 275–375 °C), Ru/ZSM-5 exhibits methane yields that increase from 92.8% at 275 °C to 98.8% at 375 °C.[39] We previously demonstrated that at lower temperature and hydrogen pressure, Ru supported on larger-pore Brønsted-acidic zeolites such as BEA or FAU produces high liquid yields with lower methane formation.[21] Wang et al. observed suppression of methane formation over Ru supported on tungstated zirconia, attributing the effect to hydrogen spillover from the support, which improves hydrogen coverage on the surface and helps desorb long alkyl intermediates to prevent them from undergoing further carbon–carbon bond cleavage to produce methane.[22] Sun et al. found that Ce-promoted Ni/BEA enhanced the selectivity towards naphtha range hydrocarbons (>80% selectivity) during polyethylene hydrocracking at 300 °C and 30 bar H$_2$, and attributed the enhanced selectivity to a mechanism involving reverse spillover of hydrogen from ceria to Ni sites.[41] The group also found that the production of coke over Ni/BEA could be prevented by the addition of ceria. These findings highlight how the choice of metal on acidic supports can steer the dominant C–C cleavage mechanism and in turn, the product distribution for polyolefin depolymerization.

Additionally, the role of water, commonly present in post-consumer plastic streams, remains poorly understood. Though water is often considered detrimental in zeolite catalysis due to acid site modification or pore blockage, recent studies suggest more nuanced effects, with reports of water altering proton transfer dynamics, stabilizing or disrupting framework structures, and mediating adsorption depending on zeolite topology and defect density.[42] For example, Kwon et al. observed enhanced LDPE conversion over Ru/zeolite-Y in the presence of water, which increased conversion from 80.6% to 96.9%.[43] This improvement was attributed to enhanced metal–acid cooperation, possibly due to increased proton mobility,

facilitated hydrogen spillover, and reduced coke formation that preserved active sites.[43]

While much of the prior work has focused on enhancing activity and selectivity, recent life cycle assessment (LCA) and techno-economic analysis (TEA) studies highlight that practical plastic upcycling technologies must also minimize energy input and rely on earth-abundant, low-cost metals to enable scalable implementation.[6,44] These considerations further motivate the development of noble-metal-free, energy-efficient catalytic systems that can advance toward industrially relevant conditions, such as the Co–Ni/BEA platform explored here.

In this study, we synthesized and characterized noble-metal-free Co–Ni/H-BEA catalysts (Si/Al = 12.5) and evaluated their performance for the hydrocracking of LDPE and a model compound, tetracosane. We explored how varying Co : Ni ratios influence hydrogen activation, product selectivity, and catalyst performance in the presence of water. Our goal is twofold: (1) to enhance hydrocracking activity and selectivity towards C_3–C_7 hydrocarbons through optimized metal–acid synergy, and (2) to reduce reliance on Co by leveraging the catalytic potential of Ni. Zeolite BEA was chosen based on its relatively large pore size and precedent for high activity in bifunctional hydrocracking reactions.[45] Catalysts were characterized using Inductively Coupled Plasma Optical Emission Spectroscopy (ICP-OES), H_2-Temperature Programmed Reduction (H_2-TPR), Scanning Transmission Electron Microscopy with Energy Dispersive X-Ray Spectroscopy (STEM-EDS), CO pulse chemisorption, X-Ray Photoelectron Spectroscopy (XPS), X-Ray Diffraction (XRD), Thermogravimetric Analysis (TGA), N_2 physisorption, and Ammonia Temperature-Programmed Desorption (NH_3-TPD). Hydrocracking reactions were performed at 265–285 °C and 15–30 bar H_2 (at 298 °C) under stirring at 450 RPM. This study provides a blueprint for designing robust, bifunctional, earth-abundant catalysts capable of operating under realistic, moisture-containing conditions, advancing the field toward scalable, sustainable plastic upcycling.

2.   Materials and methods

2.1.   Materials

The chemicals in this study were used without further purification. Low-density polyethylene (LDPE, $M_w \sim$ 4000 by GPC) was sourced from Sigma-Aldrich, and tetracosane ($C_{24}H_{50}$), 99% was obtained from Fisher Scientific. Zeolite BEA (ammonium-form, Si : Al ratio of 12.5), was procured from Zeolyst International. Cobalt(II) nitrate hexahydrate (Co $(NO_3)_2·6H_2O$) and nickel(II) nitrate hexahydrate (Ni $(NO_3)_2·6H_2O$) were obtained from Sigma-Aldrich and used as precursors for the catalyst preparation. Additional details on materials, preparation procedures, and analytical methods are provided in the SI.

2.2.   Catalyst preparation

Catalysts were synthesized *via* incipient wetness impregnation, with a total metal loading of 9 wt% and varying Co : Ni mass

ratios (1 : 2, 1 : 1, 2 : 1), as summarized in Table 1. Prior to impregnation, the H-BEA support was treated in air in a muffle furnace at 450 °C (1 °C min⁻¹) for 4.5 h. The incipient wetness point was determined by adding nanopure water dropwise to the support while mixing with a mortar and pestle until a mud-like consistency was achieved. Aqueous solutions of cobalt(II) nitrate hexahydrate (Co $(NO_3)_2·6H_2O$) and nickel(II) nitrate hexahydrate (Ni $(NO_3)_2·6H_2O$) were prepared based on the mass of support used, using the equation shown in Equation (S2) for a representative case. For Co : Ni catalysts, the precursors were mixed in a single aqueous solution before impregnation. The solutions were sonicated to ensure complete solvation in nanopure water before being added to the support. The targeted Co : Ni ratios are summarized in Table 1 and were verified by ICP-OES performed by Galbraith Laboratories.

Following impregnation, the catalysts were dried overnight at ~110 °C and subsequently treated in air at 450 °C (1 °C min⁻¹) in a muffle furnace for 4.5 h. After cooling to room temperature, the catalysts were treated in flowing argon (100 mL min⁻¹) for 5 minutes, after which hydrogen (100 mL min⁻¹) was introduced. Reduction in flowing hydrogen was performed at 450 °C for 3 h (5 °C min⁻¹). To prevent rapid oxidation of the metallic sites upon exposure to air, the catalysts were cooled to room temperature under flowing argon (100 mL min⁻¹), followed by controlled passivation in 1% O_2/Ar (100 mL min⁻¹) for 30 minutes at room temperature. This passivation step ensured safe handling and preservation of the reduced metal state prior to catalytic testing. The passivated catalysts were promptly transferred from the furnace into the batch reactor. For experiments with H-BEA and no metal loading, the catalyst was treated in air in a muffle furnace at 450 °C (1 °C min⁻¹) for 4.5 h and immediately transferred to the reactor.

2.3.   Catalyst characterization

Details for catalyst characterization, including N_2 adsorption for surface area and pore volume, XRD, H_2-TPR, CO Pulse Chemisorption, NH_3-TPD, STEM-EDS, and XPS are provided in the SI.

2.4.   Hydrocracking tests and product analysis

Catalytic hydrocracking of tetracosane and LDPE was performed in a 25 mL stainless steel Parr batch reactor with a PTFE-lined magnetic stir bar (450 RPM). A mixture of 700 mg of tetracosane or LDPE and 70 mg of catalyst was loaded into the reaction vessel. The vessel was sealed and purged three times with nitrogen followed by three times with hydrogen, then filled to a hydrogen pressure of 15, 20, or 30 bar, corresponding to initial hydrogen masses of ~44, ~60, and ~89 mg, respectively.

The temperature of the reaction was monitored using a K-type thermocouple positioned just above the melt surface. The reactor's external surface was heated using a customized heating band, and the temperature was controlled with a Parr 4838 temperature controller. The target reaction temperatures of 265 °C, 275 °C, and 285 °C were reached within 50, 80, and

Table 1 Summary of catalyst characterization obtained from ICP, N$_2$ physisorption, H$_2$-TPR, and NH$_3$-TPD

Catalyst	Co loading[a] (wt%)	Ni loading[a] (wt%)	Surface area[b] (m² gcat⁻¹)	External surface area[b] (m² gcat⁻¹)	V$_{pore}$[b] (cm³ gcat⁻¹)	Hydrogen uptake H$_2$-TPR[c] (cm³ gcat⁻¹) Total	T$_{onset}$ (°C)	Acidity NH$_3$-TPD[d] (mmol$_{NH_3}$ gcat⁻¹) Weak	Medium	Strong	Extra-strong	Total	T$_{Max, weak}$ (°C)	T$_{Max, medium}$ (°C)	T$_{Max, strong}$ (°C)	T$_{Max, extra strong}$ (°C)
H-BEA	N/A	N/A	624 ± 5	175 ± 1	0.588 ± 0.011	N/A	N/A	0.323 ± 0.051	N/A	0.410 ± 0.000	N/A	1.76 ± 0.99	198 ± 3	N/A	347 ± 5	N/A
Ni/BEA	N/A	9.00	444 ± 70	136 ± 27	0.560 ± 0.017	42.0 ± 1.3	300 ± 12	0.445 ± 0.010	0.180 ± 0.100	0.390 ± 0.000	0.310 ± 0.000	1.70 ± 0.11	165 ± 0	260 ± 0	363 ± 8	453 ± 6
Co$_1$Ni$_2$/BEA	2.64	6.07	489 ± 17	145 ± 3	0.550 ± 0.033	45.0 ± 9.1	232 ± 4	0.335 ± 0.025	0.190 ± 0.025	0.390 ± 0.000	0.300 ± 0.038	1.93 ± 0.19	172 ± 0	260 ± 0	353 ± 0	444 ± 0
Co$_1$Ni$_1$/BEA	4.57	4.43	529 ± 31	157 ± 8	0.572 ± 0.026	46.6 ± 8.9	228 ± 4	0.405 ± 0.015	0.270 ± 0.150	0.510 ± 0.000	0.210 ± 0.000	2.43 ± 0.44	167 ± 0	260 ± 0	386 ± 21	480 ± 0
Co$_2$Ni$_1$/BEA	6.15	2.50	473 ± 12	140 ± 2	0.567 ± 0.031	46.3 ± 4.0	236 ± 15	0.322 ± 0.000	0.280 ± 0.030	0.440 ± 0.000	0.240 ± 0.018	1.88 ± 0.10	170 ± 0	260 ± 0	390 ± 0	463 ± 0
Co/BEA	8.82	N/A	350 ± 34	105 ± 10	0.457 ± 0.068	50.1 ± 5.9	262 ± 4	0.287 ± 0.016	0.290 ± 0.037	0.470 ± 0.000	0.370 ± 0.000	2.01 ± 0.00	180 ± 0	260 ± 0	390 ± 0	460 ± 0

[a] Confirmed by Inductively Coupled Plasma-Optical Emission Spectroscopy (ICP-OES). [b] Measured by Brunauer–Emmett–Teller (BET) surface area analysis. [c] Quantified by Hydrogen Temperature Programmed Reduction (H$_2$-TPR). [d] Measured by Ammonia Temperature Programmed Desorption (NH$_3$-TPD). Additional catalyst characterization data and experimental procedures are provided in the SI. Results represent an average across two experiments for each catalyst.

100 minutes, respectively. At the end of the reaction, the reactor was immediately cooled to room temperature by removing the vessel from the heater and blowing ambient air over the reactor body. Once the system reached room temperature, gaseous products were collected in a gas bag and mixed with CO$_2$ as an internal standard for analysis. The reactor was then cooled to approximately 9 °C using an ice bath to minimize the loss of volatile liquid hydrocarbons. Liquid products were dissolved in toluene or cyclohexane with tri-tertbutyl benzene as an internal standard. Control reactions performed in the absence of catalyst confirm no intrinsic activity of the reactor walls (Fig. S23).

Gaseous and liquid products were identified and quantified using a custom gas chromatography suite including an Agilent 8890 gas chromatography equipped with a thermal conductivity detector (GC-TCD) and a flame ionization detector (GC-FID), and a gas chromatograph equipped with a mass spectrometer (MS). Additional details for product identification and quantification methods and conversion calculations are provided in the SI. For experiments that initially exhibited low mass balances, we employed an alternative gas-collection method developed by Brenner et al.[46] to improve overall mass balance recovery and ensure fair comparison with experiments that achieved higher mass balances.

3. Results and discussion

3.1. Catalyst characterization

The catalyst characterization is summarized in Table 1. The parent H-BEA zeolite (Si : Al 12.5) exhibits a relatively high BET surface area (~624 m² gcat⁻¹). Upon metal incorporation, a significant decrease in surface area is observed for both 9 wt% Co/BEA (Co/BEA) (~350 m² gcat⁻¹) and 9 wt% Ni/BEA (Ni/BEA) (~444 m² gcat⁻¹). This is attributed to partial pore blockage and surface coverage by metal nanoparticles, as suggested by concurrent decreases in BET surface area, pore volume, and external surface area. Such declines are consistent with prior studies on Pt/H-BEA, where surface area dropped from 485 to 407 m² gcat⁻¹ upon Pt introduction due to similar obstruction effects.[47] The pronounced reduction in external surface area for monometallic samples (e.g., ~105 m² gcat⁻¹ for Co/BEA) suggests that metal nanoparticles may reside at or near pore entrances, or in some cases within larger pores, partially restricting access. This is similar to observations in Ni/Al$_2$O$_3$ catalysts where surface area and pore size decreased due to nanoparticle penetration into mesoporous channels.[27] In contrast, the bimetallic Co$_1$Ni$_1$/BEA catalyst retains a higher surface area (~529 m² gcat⁻¹) and external surface (~157 m² gcat⁻¹), suggesting improved metal dispersion. N$_2$ isotherms (Fig. S2) show greater N$_2$ uptake across both micropore and mesopore regions relative to Co/BEA. These improvements align with prior work by Gebresillase et al., who reported that Ni–Co/γ-Al$_2$O$_3$ catalysts exhibited higher BET surface area, larger pore volume, and smaller Ni crystallite sizes compared to monometallic Ni catalysts, indicating improved metal dispersion and better retention of porosity.[48]

The hydrogen temperature-programmed reduction (H$_2$-TPR) profiles of the catalysts (Fig. 1a and 2a) reveal distinct reduction behaviors among the mono- and bimetallic systems. The Co/BEA catalyst exhibits the highest total hydrogen uptake ($\sim$50.1 cm^3 g$_{cat}^{-1}$), accompanied by broad reduction peaks centered at approximately 297 °C, 465 °C, and 640 °C. These features correspond to the sequential reduction of Co$_3$O$_4$ to Co^0 through intermediate Co^{3+} to Co^{2+} and Co^{2+} to Co^0 transitions, as previously reported for Co$_3$O$_4$ systems.[36] In contrast, Ni/BEA shows more defined peaks at 345 °C and 563 °C, associated with the reduction of Ni^{2+} species (primarily dispersed NiO) to metallic Ni. The bimetallic Co$_1$Ni$_1$/BEA sample displays broader and more intense peaks, with a significantly lower T_{onset} at 228 °C. This suggests enhanced reducibility arising from synergistic effects: Ni facilitates Co reduction, while Co boosts hydrogen uptake in Ni-containing systems. These findings are consistent with previous work by Hernández Mejía et al., who attributed the enhanced reducibility of Ni–Co oxide systems to synergistic effects related to the presence of mixed oxide phases, rather than changes in electronic structure.[36] Yao et al. observed similar effects in Ni–Cu systems, and provided direct spectroscopic evidence of hydrogen spillover from Ni to adjacent metal phases on reducible oxides.[49]

The NH$_3$-TPD profiles (Fig. 1b) elucidate how cobalt and nickel incorporation alter the acidic properties of H-BEA. Compared to the parent zeolite, metal-modified catalysts show broadened ammonia desorption peaks and the emergence of high-temperature features in the 350–550 °C range, indicative of stronger acid sites. Deconvoluted NH$_3$-TPD curves are shown in Fig. S5. Quantitative analysis reveals that Ni/BEA pos-
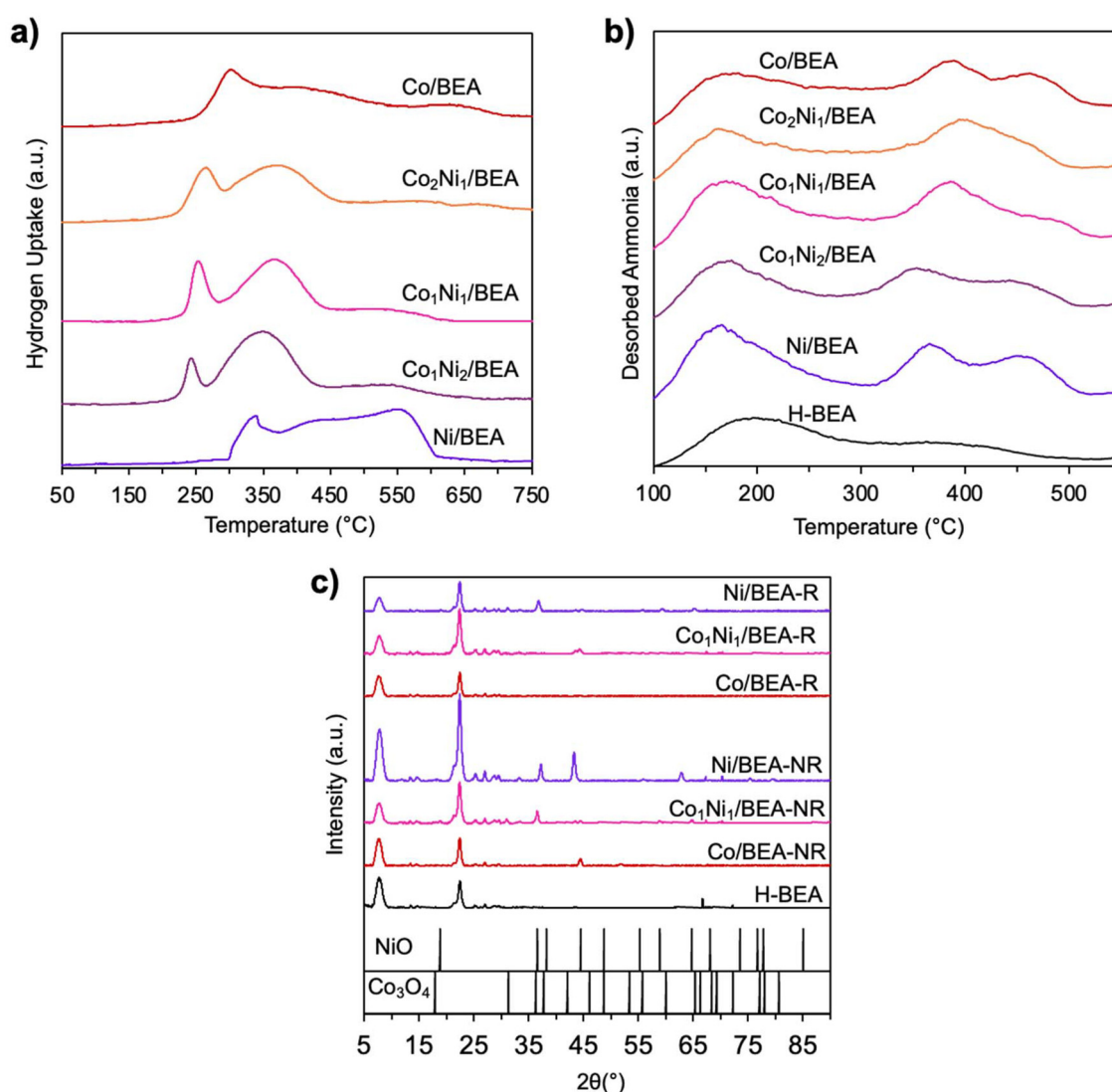

Fig. 1 (a) H$_2$-TPR profiles showing hydrogen uptake as a function of temperature for monometallic and bimetallic Co−Ni/BEA catalysts that have not been previously reduced. (b) NH$_3$-TPD profiles of the catalysts showing desorption behavior corresponding to different acid site strengths. (c) XRD patterns of fresh catalysts, highlighting crystalline phases attributed to metallic and oxide species as well as BEA framework reflections (R = reduced catalyst, NR = not reduced catalyst). The bottom spectra correspond to reference patterns for Co$_3$O$_4$ and NiO.
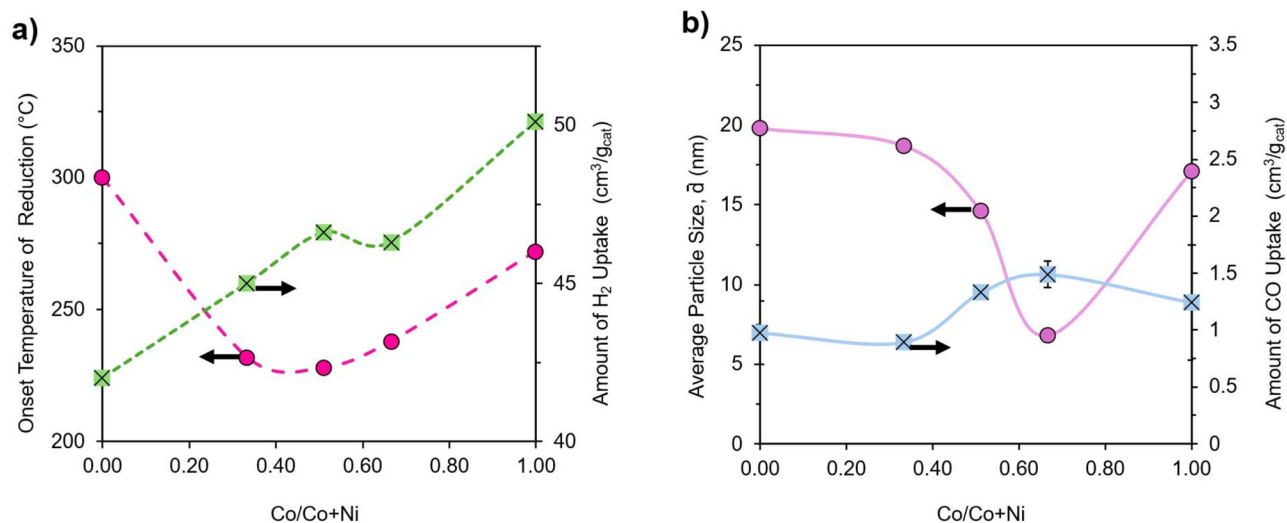
Fig. 2 (a) Total hydrogen uptake (cm³ g$_{cat}^{-1}$) and onset temperature of reduction (T_{onset}) derived from H$_2$-TPR data. (b) Average particle diameter ($\bar{d}$) plotted against CO uptake as a function of Co/(Co + Ni) ratio.

sesses the highest concentration of weak acid sites (0.45 mmol NH$_3$ per g$_{cat}$), while Co/BEA is rich in extra-strong acid sites (0.37 mmol NH$_3$ per g$_{cat}$). The bimetallic Co$_1$Ni$_1$/BEA catalyst has the highest total acidity (2.43 mmol NH$_3$ per g$_{cat}$), with significantly higher contributions from medium and strong acid sites, suggesting that synergistic interactions between Co and Ni modify the acidity profile. EDS elemental analysis (Table S1) shows a slight increase in the Si/Al molar ratio after metal loading, from 12.50 in pristine H-BEA to 13.42–15.19 in metal-containing samples, indicating partial dealumination during synthesis and/or reduction. This shift may suggest the formation of extra-framework aluminum species and altered acid environments. These observations are consistent with prior studies on BEA and ZSM-5, which show that post-synthetic treatments leading to framework disruption generate extra-framework Al species (EFAl) (*e.g.* Al^{3+}, AlO$^+$, Al(OH)$_2^+$, AlOH$_2^+$) that behave as strong Lewis acid sites. For example, steaming-induced EFAl formation in H-BEA and H-ZSM-5 enhances Friedel–Crafts acylation rates, whereas removal of EFAl decreases activity, indicating that these Lewis sites contribute significantly alongside framework Brønsted sites.[50,51] In our system, the emergence of high-temperature NH$_3$ desorption may be attributed to similar mechanisms, where Co and Ni promote the formation of Lewis acid sites that may enhance hydrocracking performance.

X-ray diffraction patterns (Fig. 1c and Fig. S8b, c) confirm that the BEA zeolite framework remains structurally intact after metal incorporation and H$_2$ reduction, with characteristic reflections at 7.6° and a broad envelope between 22.5–25.5°. In the as-prepared (not reduced, NR) Co$_1$Ni$_1$/BEA catalyst, additional peaks at 31.3°, 36.8°, 44.8°, 59.3°, and 65.2° are consistent with Co$_3$O$_4$, while peaks at 37.2°, 43.3°, and 62.9° can be assigned to NiO. These peaks disappear after reduction, suggesting transformation of metal oxides to their metallic states. The absence of distinct Co^0 or Ni^0 peaks in the reduced

samples (expected near 44–46° and 51–52°)[52,53] can be rationalized by a combination of high metal dispersion which forms small crystallites below the XRD detection threshold, and potential overlap with intense BEA framework peaks. These observations are consistent with prior reports of highly dispersed Ni–Co systems, where metallic signatures are often obscured.[54]

High-angle annular dark-field scanning transmission electron microscopy (HAADF-STEM) images (Fig. 3a–f) further support improved metal dispersion in bimetallic catalysts. The Co$_1$Ni$_1$/BEA catalyst shows a relatively uniform particle size of 14.6 nm, smaller than those of Co/BEA (17.1 nm) and Ni/BEA (19.8 nm). Increasing Co content in Co$_2$Ni$_1$/BEA further reduces the particle size to 6.8 nm, whereas increasing the Ni content in Co$_1$Ni$_2$/BEA results in a larger average size of 18.7 nm. This enhanced dispersion may arise because introducing Ni into Co/BEA, or Co into Ni/BEA, disrupts the preferred crystallite growth pathways of the primary metal, suppresses agglomeration, and stabilizes finer particles. A similar effect was observed for Ni–Fe/Al$_2$O$_3$, where adding Fe reduced Ni particle size from 14.21 nm to 12.74 nm by disrupting Ni crystallite growth and suppressing agglomeration, leading to improved catalytic performance in polyethylene hydrogenolysis.[27] Consistent with these TEM trends, Scherrer analysis of the XRD patterns (Table S4) also indicates the smallest crystallite sizes for Co$_2$Ni$_1$/BEA (7.1 nm) and Co$_1$Ni$_1$/BEA (7.7 nm), compared with larger sizes for monometallic Co (16.3 nm) and Ni (19.4 nm). Full details of the Scherrer equation estimated parameters are provided in the SI.

EDS line scans (Fig. S1c) reveal spatially distinct distributions of Co and Ni, suggesting partial phase segregation. This is further supported by XPS analysis (Fig. S10), which shows a higher surface concentration of Co relative to Ni and a weak Ni 2p signal in Co$_2$Ni$_1$/BEA, consistent with lower Ni surface exposure.

The average particle sizes collected across the images in Fig. 3a–e for each sample are plotted in Fig. 2b alongside measurements of CO uptake from CO Pulse Chemisorption measurements (Table S3), which provides a bulk measure of dispersion. CO pulse chemisorption results are consistent with the particle size trends, where the catalysts with the smallest particles have the highest uptake, indicating higher concentration of exposed metal sites for CO adsorption, and higher dispersion. All catalysts exhibit gradual uptake over 10 pulses, consistent with weakly adsorbed CO and surface site crowding (Fig. S6). In this study, the use of 10 CO pulses under standardized conditions helps minimize physisorption and saturation artifacts. While some degree of physisorption is inevitable, this approach provides a qualitative assessment of metal dispersion and surface accessibility, rather than an absolute measure. Bimetallic catalysts display higher CO uptake than their monometallic analogues, indicating improved dispersion and greater metal surface accessibility. Among them, Co_2Ni_1/BEA shows the highest CO uptake, consistent with its smallest particle size, highlighting the inverse relationship between size and accessible metal surface area. This trend underscores the role of Co–Ni synergy in suppressing agglomeration and stabilizing finely dispersed active phases. An exception to this size–uptake correlation is Co/BEA, which despite having larger

particles (~17 nm) exhibits uptake values comparable to Co_2Ni_1/BEA. This anomaly may be explained by differences in CO binding strength between Co and Ni. Recent DFT calculations by Perilli *et al.* demonstrated that CO binds more strongly to Co than Ni, as the Co d_{xz}/d_{yz} orbitals lie at the Fermi level and enable strong π-backdonation into the CO antibonding orbitals, whereas the corresponding Ni orbitals are buried deeper, suppressing CO adsorption.[55] This intrinsic difference in binding affinity helps explain why Co/BEA maintains relatively high CO uptake despite its larger particle size. Overall, combined STEM-EDS and chemisorption analyses confirm that Co–Ni bimetallic catalysts achieve superior metal dispersion, suggesting that the presence of both metals limits crystal growth of either phase, producing smaller particles and more accessible active sites.

3.2. Catalytic hydrocracking of LDPE and tetracosane into liquid hydrocarbon fuels

The catalytic performance of mono- and bimetallic Co–Ni catalysts supported on BEA was first evaluated for the hydrocracking of tetracosane in batch reactors at 265 °C, 20 bar H_2 (~47 bar at 265 °C), 3 h, using 70 mg of catalyst with 700 mg of substrate. The yields and product distributions of liquid and gaseous hydrocarbons, hydrogen conversion, and tetracosane
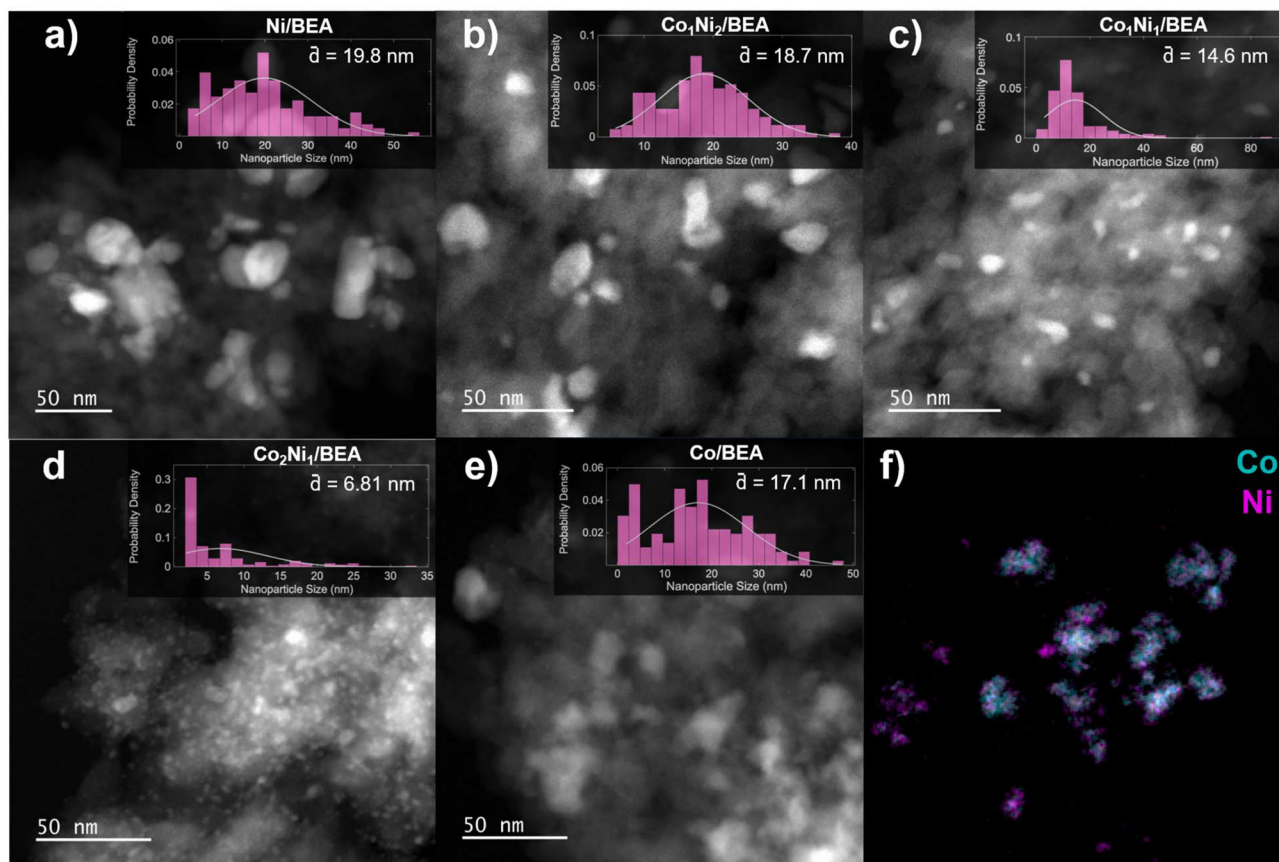

Fig. 3 (a–e) HAADF-STEM images for (a) Ni/BEA, (b) Co_1Ni_2/BEA, (c) Co_1Ni_1/BEA, (d) Co_2Ni_1/BEA, and (e) Co/BEA, with insets showing nanoparticle size distributions. (f) Elemental maps showing Co (cyan) and Ni (magenta) distributions for Co_1Ni_1/BEA.

conversion across the series of Co–Ni/BEA catalysts are shown in Fig. 4. While tetracosane conversion is nearly 100% across the entire series, the inclusion of metal sites significantly increased hydrogen conversion compared to H-BEA alone, which showed the lowest hydrogen conversion (~11%). In contrast, the bimetallic Co_1Ni_1/BEA catalyst demonstrated the highest hydrogen conversion (~50%), outperforming both Ni/BEA (~34%) and Co/BEA (~37%).

Product distribution analyses revealed key differences between metal-free and metal-containing catalysts (Fig. 4b–g). H-BEA alone predominantly yielded heavier hydrocarbons and unsaturated alkanes, which are expected products of monofunctional acid catalysis, where β-scission generates reactive olefins that, without sufficient hydrogenation, can undergo oligomerization or repolymerization into heavier products including carbonaceous deposits. This contrasts with recent findings by Tan et al., who reported higher activity for metal-free MFI zeolites compared to zeolites loaded with 1 wt% Pt or Ni in polyethylene hydrocracking, attributed to shape-selective confinement of the 10-membered ring framework.[26] While Tan et al. reported that metal incorporation into MFI suppressed polyethylene conversion due to preferential alkene hydrogenation, the differences with the larger-pore BEA framework suggest that pore architecture can mediate how metals influence the hydrocracking pathway for long-chain

intermediates.[26] In our system, the larger-pore H-BEA framework (12-membered ring) appears to benefit from metal incorporation: Co- and Ni-containing catalysts favored the formation of lighter C_4–C_{10} alkanes. Ni selectively promotes mid-chain C–C cleavage toward internal alkanes, whereas Co favors CH_4 formation (~5 mg). This aligns with hydrogenolysis studies where Co-rich surfaces cleave terminal bonds and promptly hydrogenate CH_x intermediates, generating methane.[17] For comparison, a Ru/BEA catalyst (9 wt%) was synthesized and evaluated under identical conditions, with hydrocracking results shown in Fig. S24(a–c) and corresponding Ru/BEA characterization in Fig. S25(a and b). Under these conditions, the extensive methane formation emphasizes the advantages of earth-abundant Co–Ni/BEA for selective formation of liquid-range alkanes. While the mechanism differs from Fischer–Tropsch synthesis, Todic et al. modeled similar secondary methane formation via rapid hydrogenation of surface CH_x species on Co catalysts,[56] reinforcing the link between the hydrogenation ability of CO and methane selectivity. Turnover-based metrics (Table S9) further highlight this trend: among all Co–Ni/BEA compositions, the 1 : 1 Co/Ni catalyst exhibited the highest activity when normalized to total metal loading, consistent with its superior hydrogen activation and balanced hydrocracking–hydrogenolysis behavior.
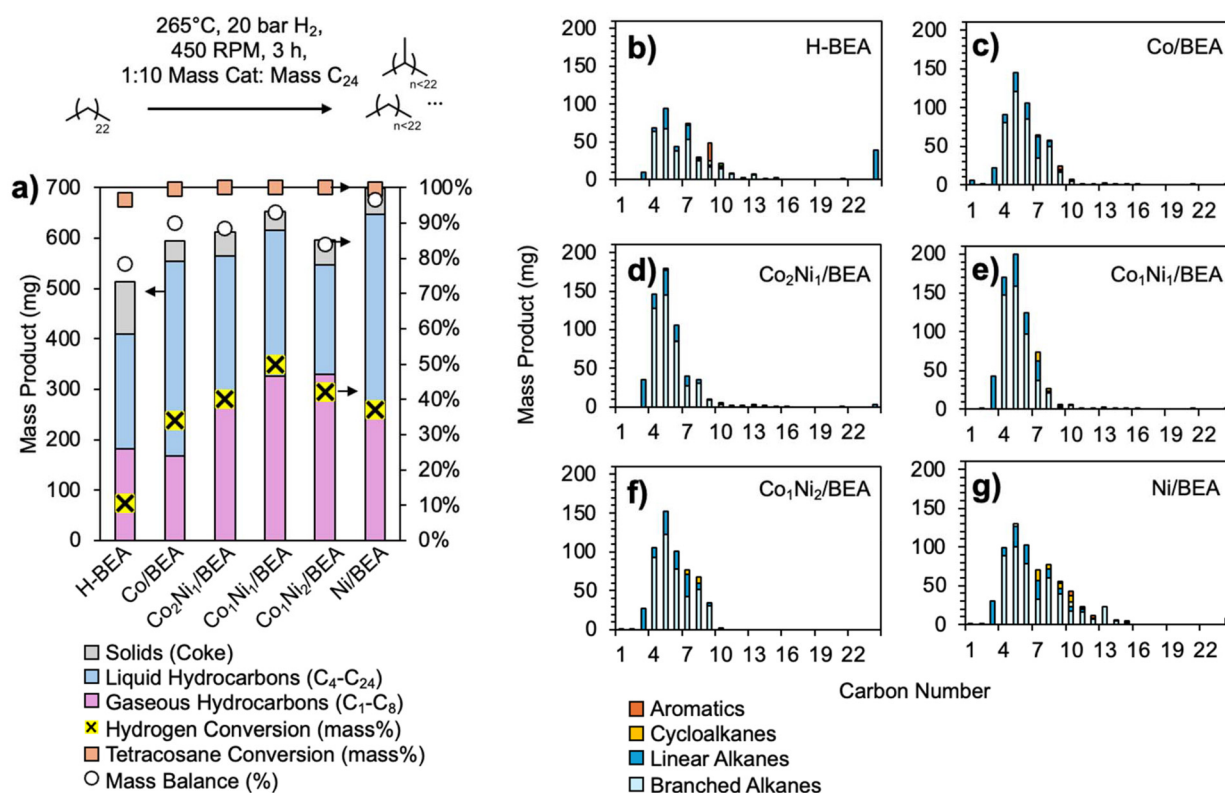

Fig. 4 (a) Product yields from tetracosane hydrocracking over H-BEA, Co/BEA, Co_2Ni_1/BEA, Co_1Ni_1/BEA, and Co_1Ni_2/BEA catalysts, with overlaid mass balance, tetracosane conversion, and hydrogen conversion on the secondary y-axis (700 mg substrate, 70 mg catalyst, 3 h reaction), (b–g) carbon number distribution (C_1–C_{20+}) of products categorized as aromatics (orange), cycloalkanes (yellow), linear alkanes (dark blue), and branched alkanes (light blue).

Coke formation was assessed *via* thermogravimetric analysis (Fig. S7) before and after the reactions. Among the catalysts, H-BEA showed the greatest mass loss, consistent with the absence of metal sites to hydrogenate reactive intermediates. In acid-only systems, β-scission generates olefinic fragments that can undergo secondary reactions such as cyclization, aromatization, and polycondensation, ultimately leading to polyaromatic coke deposits.[57,58] In contrast, all metal-containing catalysts (Co–Ni/BEA) exhibited lower coke deposition, with most mass loss occurring in the soft coke region. The presence of metals provides a parallel hydrogenation pathway, saturating olefinic and aromatic intermediates before they can repolymerize into condensed coke structures. These results underscore the necessity of metal sites for promoting hydrogenation and mitigating condensation pathways, thereby improving resistance to coke formation.

Further comparisons among Co/Ni ratios (2 : 1, 1 : 1, 1 : 2) demonstrated that the 1 : 1 Co–Ni ratio (Co$_1$Ni$_1$/BEA) achieved the highest hydrogen conversion and yield of lighter alkanes while completely suppressing CH$_4$ formation (Fig. 4d–f). TGA results showed minimal coke formation across all bimetallic compositions, suggesting improved resistance to deactivation (Fig. S7). Previous studies have shown that equimolar Co–Ni systems often exhibit enhanced reducibility and strong metal–metal synergy, which improve reduction properties and facilitate co-reduction.[36,59] Consistent with these reports, H$_2$-TPR analysis (Fig. 1a) reveals a lower reduction onset temperature (T_{onset}) and broad H$_2$ uptake for Co$_1$Ni$_1$/BEA, suggesting the formation of a bimetallic surface which excels at hydrogen activation. Altogether, Co–Ni bimetallic catalysts demonstrate superior performance, with the 1 : 1 composition offering an optimal balance between activity, selectivity, and stability. Control reactions with Co, Ni, and Co : Ni 1 : 1 dispersed on amorphous silica with the same total weight loading were also performed and demonstrated little to no activity under conditions of 265 °C, 20 bar H$_2$, 3 h, (Fig. S26), highlighting the importance of the acid sites for hydrocracking.

To assess the impact of metal site intimacy and interaction, a co-impregnated Co$_1$Ni$_1$/BEA catalyst was compared to a physical mixture of Co/BEA and Ni/BEA prepared under identical conditions. As shown in Fig. 5a, the co-impregnated catalyst achieved higher hydrogen conversion (50%) compared to the physical mixture (37%). Furthermore, the physically mixed catalyst generated ~7 mg of methane (Fig. 5c), a product absent in the co-impregnated system. The inferior performance of the physical mixture likely stems from spatial separation between Co and Ni, which limits hydrogen spillover and the stabilization of reactive intermediates.

XPS analysis revealed no significant shifts in the binding energies of Co or Ni (Fig. S9 and S10) from monometallic to bimetallic, which would suggest the absence of electronic structure modification; however, surface oxidation may obscure these effects. The observed synergy could also be attributed to physical proximity and hydrogen spillover rather than electronic effects. Supporting this, H$_2$-TPR profiles (Fig. S4) show a significantly lower reduction onset (~228 °C) and broad hydro-
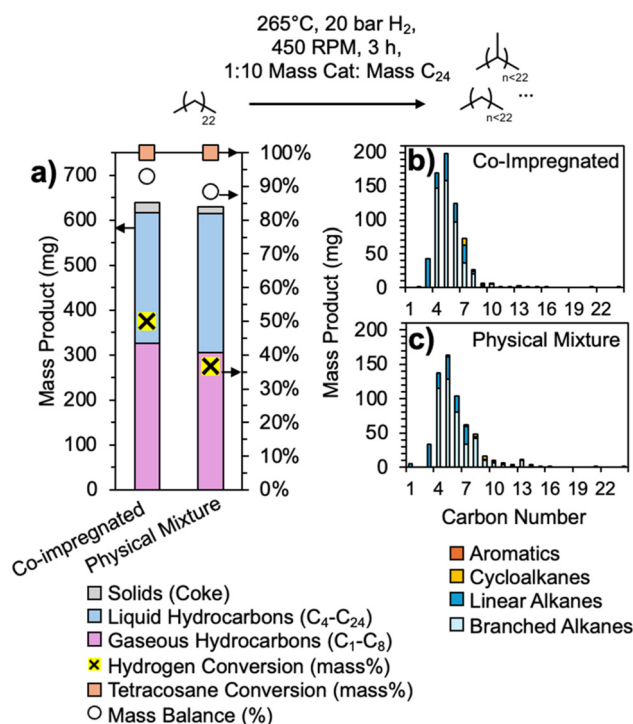

Fig. 5 (a) Product yields from tetracosane (700 mg) hydrocracking over a physical mixture of Co/BEA and Ni/BEA (~35 mg each) and co-impregnated Co$_1$Ni$_1$/BEA (~70 mg), with overlaid mass balance, tetracosane conversion, and hydrogen conversion. (b and c) Carbon number distribution (C$_1$–C$_{20+}$) of products, categorized as aromatics (orange), cycloalkanes (yellow), linear alkanes (dark blue), and branched alkanes (light blue).

gen uptake for the co-impregnated sample, indicating enhanced reducibility. In comparison, the physical mixture displays broader, less-resolved peaks resembling a superposition of monometallic profiles, consistent with minimal Co–Ni interaction. Similar proximity-driven metal cooperation has been reported by Hou *et al.*, where Rh addition to Co/ZSM-5 improved catalytic performance through hydrogen spillover and enhanced dispersion, rather than through electronic modification.[60]

It is important to note that these hydrocracking processes proceed *via* both parallel and series reactions, where solids break down into liquids, which then break down into gas. As hydrogen conversion increases, so does the fraction of light hydrocarbons. For reactions in which the products are primarily saturated alkanes, it can be assumed that every H$_2$ consumed is one carbon–carbon bond broken. Thus, to enable a fair comparison of intrinsic selectivity, reactions were performed with varying reaction times to reach an equivalent hydrogen conversion of ~51 ± 3%. The bimetallic Co$_1$Ni$_1$/BEA achieved this within 3 h, faster than both Co/BEA (4 h) and Ni/BEA (4.5 h) (Fig. 6a), highlighting the superior efficiency of the bimetallic system. Product selectivity also differed across the catalysts: Co/BEA showed highest light gas (C$_4$–C$_5$) selectivity and ~11 mg of CH$_4$ alongside ~270 mg of liquid (C$_4$–C$_{24}$) pro-
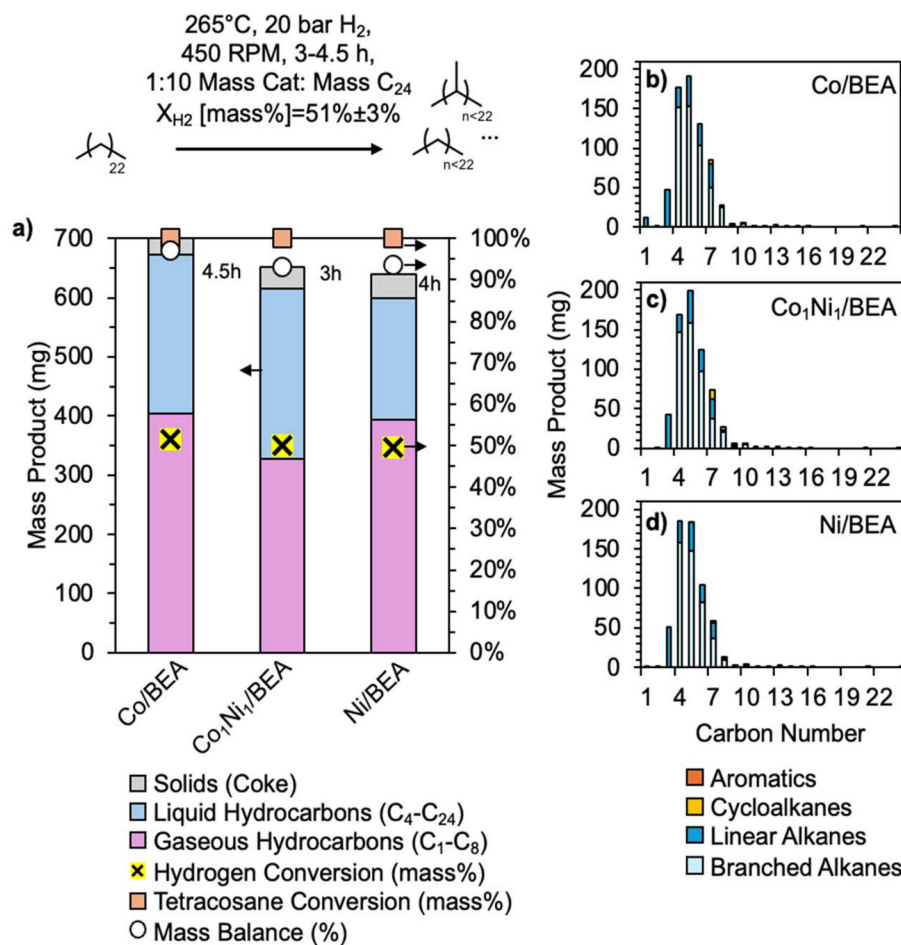
Fig. 6 Catalytic performance at equivalent hydrogen conversion. (a) Product yields from tetracosane hydrocracking over Co/BEA, Ni/BEA, and Co$_1$Ni$_1$/BEA catalysts at ~51% hydrogen conversion, with overlaid mass balance and tetracosane conversion (700 mg substrate, 70 mg catalyst), (b–d) carbon number distribution (C$_1$–C$_{20+}$) of products from Ni/BEA, Co$_1$Ni$_1$/BEA, and Co/BEA, respectively, categorized as aromatics (orange), cycloalkanes (yellow), linear alkanes (dark blue), and branched alkanes (light blue).

ducts (Fig. 6d). This is consistent with Borkar *et al.*, who found that higher Co loadings (~10 wt% Co/SiO$_2$) promoted extensive hydrogenolysis and gaseous products, whereas lower loadings (~1–5 wt%) favored liquid and solid retention during polyethylene hydrocracking at 275 °C and 30 bar H$_2$.[17] Our Co/BEA catalyst (9 wt%) falls into this high-loading regime, and HAADF-STEM analysis confirmed the presence of relatively large Co domains (Fig. 3e, 17.1 nm). In contrast, the introduction of Ni disrupts Co crystallite growth pathways, yielding smaller and more uniformly dispersed particles (Fig. 3c, 14.6 nm for Co$_1$Ni$_1$/BEA), which mitigates deep hydrogenolysis and suppresses methane formation, in agreement with the improved liquid selectivity of the bimetallic system. In contrast, Ni/BEA generated no CH$_4$ despite a comparable total gas yield. However, the lower liquid yield (~205 mg) may be attributed to excessive scission producing short-chain alkanes (C$_3$–C$_5$) that remain in the gas phase under reaction conditions, rather than condensing as liquid products. This is consistent with previous work by Vance *et al.*, who demonstrated that Ni/SiO$_2$ catalysts promote non-terminal C–C bond cleavage but

can also over-crack longer hydrocarbon chains, leading to lower liquid product yields and formation of light gases, with a small amount of methane.[16] The bimetallic catalyst delivered the most desirable selectivity profile, achieving the highest liquid product yield (~290 mg) while simultaneously suppressing methane formation. Here, Ni appears to mitigate the tendency of Co to promote deep hydrogenolysis: by dispersing Co domains and supplying activated hydrogen through spillover, Ni moderates hydrogen coverage on Co surfaces, preventing over-hydrogenation of CH$_x$ intermediates that would otherwise desorb as methane. A similar stabilization effect has been reported by Wang *et al.* in CO$_2$ hydrogenation, where Ni incorporation into Co catalysts suppressed methanation by stabilizing *CH$_x$ intermediates.[61] Taken together, these results demonstrate that tuning the Co/Ni ratio enables control over product distribution, suppresses methane, and maximizes liquid yield, underscoring the pivotal role of bimetallic synergy in efficient hydrocracking.

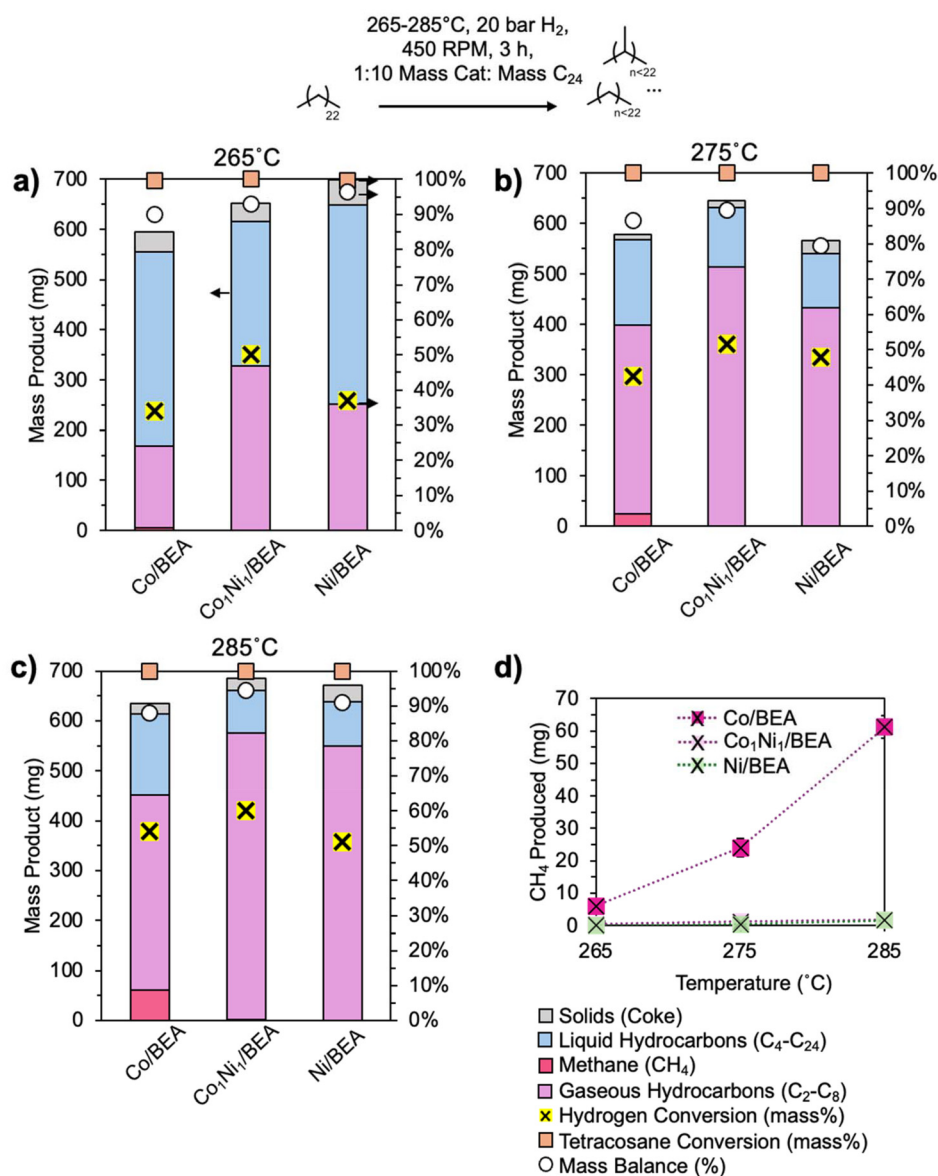To investigate the activation barriers for methane formation, we evaluated Co/BEA, Ni/BEA, and Co$_1$Ni$_1$/BEA at

Fig. 7 Temperature-dependent hydrocracking performance. (a–c) Product distribution (methane, C_2–C_8 gas, C_4–C_{24} liquid, solid) from tetracosane hydrocracking at 265 °C, 275 °C, and 285 °C over Co/BEA, Ni/BEA, and Co_1Ni_1/BEA (700 mg substrate, 70 mg catalyst, 3 h reaction). (d) Methane yield as a function of temperature for all catalysts. Detailed product distributions are provided in the SI.

temperatures ranging from 265 °C to 285 °C. Methane formation increased with temperature for Co/BEA (Fig. 7, and Fig. S27a and d), whereas neither Ni/BEA nor Co_1Ni_1/BEA produced methane at any temperature (Fig. 7a–d and Fig. S27b,c, e–f), confirming that incorporation of Ni suppresses the methane formation introduced by Co. While increasing temperature decreased liquid yields and increased gas formation across all catalysts (Fig. 7a–c), Co_1Ni_1/BEA uniquely combined methane suppression with high C_3–C_5 selectivity (Fig. 7c and Fig. S27e), demonstrating controlled mid-chain cracking with an ideal balance of Co and Ni sites. In contrast, the performance of Co/BEA performance at 285 °C yielded the highest methane among all tested catalysts (~55 mg).

The addition of Ni to Co improves the reducibility and selectivity of the reaction. This could be explained by two possible scenarios: (1) the Ni is modifying the electronic structure of the Co, thus changing the adsorption strength of the polyethylene and thus preventing over-adsorption and subsequent hydrogenolysis to methane, or (2) as proposed earlier, the Ni promotes hydrogen activation and spillover, increasing the surface concentration of H_2 and thus preventing methanation. It has been shown with Ru-based catalysts that the hydrogenolysis reaction is both promoted and inhibited by hydrogen. While higher hydrogen pressures inhibit adsorption of alkanes, they also help prevent over-hydrogenolysis to methane by preventing "deep hydrogenolysis" cleavage mechanisms,
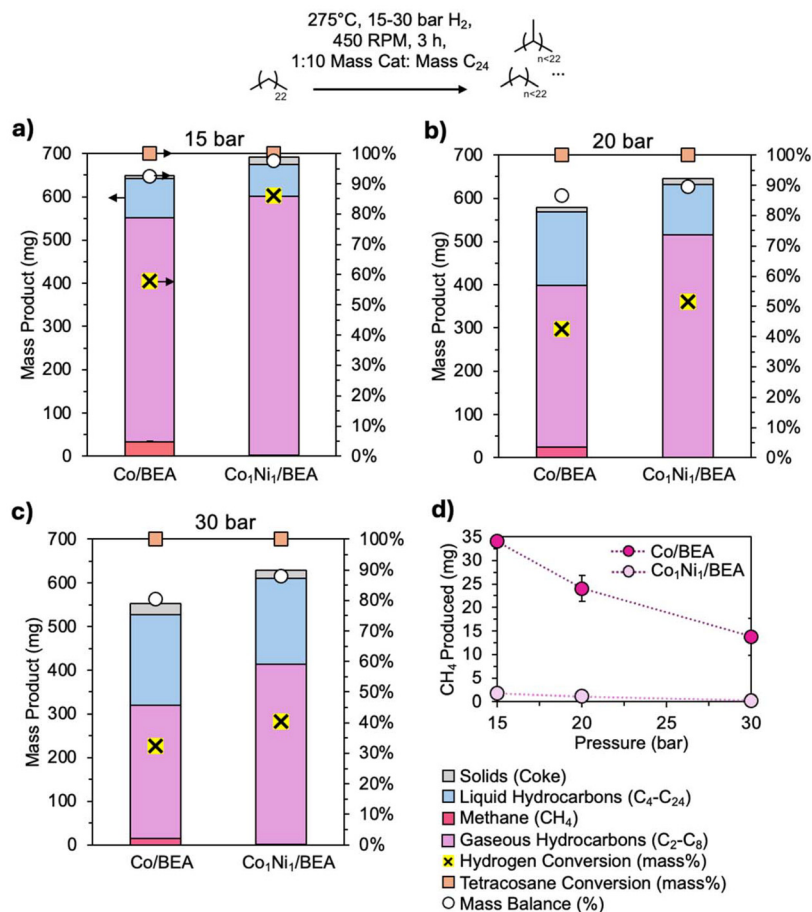
Fig. 8 Effect of hydrogen pressure on catalytic performance. (a–c) Product yields and phase distribution (gas, liquid, solid) from tetracosane hydrocracking over Co/BEA and Co$_1$Ni$_1$/BEA at 275 °C under 15, 20, and 30 bar H$_2$ (700 mg substrate, 70 mg catalyst, 3 h reaction), (d) methane yield as a function of hydrogen pressure for both catalysts. Detailed product distributions are provided in the SI.

where the alkane or polymer chain remains on the surface and undergoes multiple sequential cleavage steps, producing methane from the center of the chain. It is desirable to have a catalyst which can maintain the ideal surface coverage of hydrogen without resorting to high pressures.

To distinguish between these two potential scenarios, we took a closer look at the X-Ray Photoelectron Spectroscopy (XPS) results to consider the impact of Ni on Co electronic structure and investigated the impact of hydrogen pressure on methane formation. The XPS showed surface enrichment of Co with subsurface Ni, supporting a spatially segregated architecture enabling cooperative effects rather than uniform alloying (see SI for details). The XPS results did not, however, indicate a significant change in electronic structure of Co upon addition of Ni, as shown in Fig. S9–S15 in the SI. Yet, this could be due to surface oxidation of the samples and does not preclude strong interfacial interactions. While the absence of major shifts in binding energy or satellite features suggests that extensive alloying is unlikely, the performance improvements may stem from spatial proximity between Ni and Co domains that facilitate non-electronic cooperative effects, such

as hydrogen spillover. This is further suggested by the Co and Ni phase segregation observed *via* STEM-EDS. To support the hypothesis that the addition of Ni promotes hydrogen coverage, the impact of hydrogen pressure on reaction selectivity and activity was measured.

By varying H$_2$ pressure (15, 20, and 30 bar at room temperature, corresponding to 24, 33, and 50 bar at 275 °C, respectively), we aimed to assess how hydrogen availability influences methane formation, and whether Ni incorporation alters hydrogen utilization through mechanisms such as spillover. The temperature of 275 °C was selected to observe both methane and products of central C–C bond cleavage. Product distributions (Fig. 8a–c and Fig. S28a–d) and methane formation as a function of pressure (Fig. 8d) highlight differences in catalytic behavior. At 15 bar, both catalysts favored C$_3$–C$_5$ formation, while increasing the pressure to 30 bar shifted selectivity toward C$_5$–C$_8$ and enhanced liquid yield. The presence of small-chain alkanes in addition to methane in the case of Co/BEA suggests that methane formation arises not only from terminal C–C scission but also from over-hydrogenolysis of mid-chain fragments when the surface coverage of
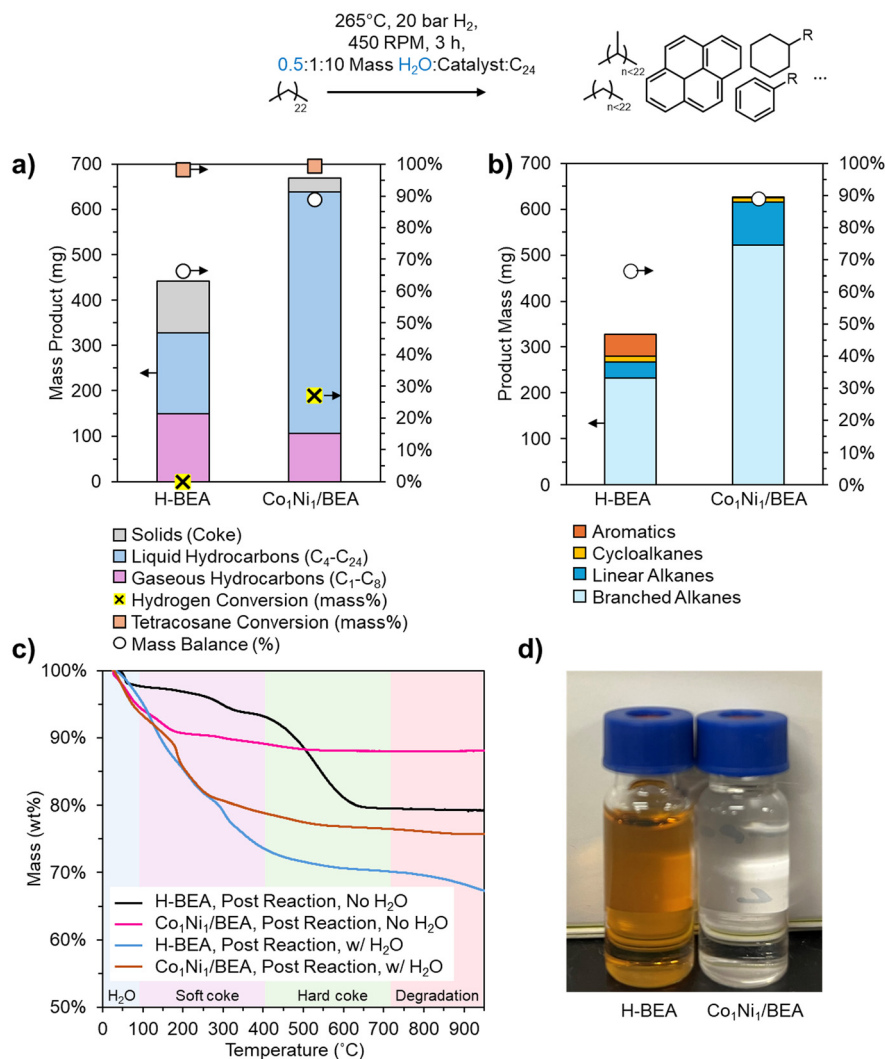
Fig. 9 Effect of water on catalytic performance and product distribution. (a) Product yield and phase distribution from tetracosane hydrocracking under wet conditions (0.5 : 1 H_2O : catalyst, 700 mg substrate, and 70 mg catalyst) over 3 h at 265 °C, 20 bar H_2, (b) hydrocarbon type selectivity categorized as aromatics, cycloalkanes, linear alkanes, and branched alkanes, (c) TGA profiles of spent catalysts after dry and wet reactions, (d) visual comparison of post-reaction organic phases after extraction in cyclohexane for H-BEA (left) and Co_1Ni_1/BEA (right).

hydrogen is too low. Based on these observations, the structural arrangement of Ni and Co domains likely enables functional separation: Ni activates H_2, generating mobile H* species that spill over to surface Co or acid sites. This moderates hydrogenation intensity during C–C cleavage, preventing over-reduction of CH_x intermediates and thereby suppressing methane formation, even with Co as the more active scission site.

While the previous sections demonstrate the effectiveness of Co–Ni/BEA under anhydrous conditions, real-world plastic streams often contain moisture. Therefore, understanding catalyst behavior in the presence of water is essential to evaluating long-term viability and robustness for practical application. Co_1Ni_1/BEA was selected for comparison with H-BEA to assess water tolerance. Hydrocracking reactions were performed under "wet" conditions (0.5 : 1 mass H_2O : catalyst) at

265 °C and 20 bar H_2 for 3 h to observe the impact of water on catalyst activity, product selectivity, and coke formation (Fig. 9). Catalytic performance (Fig. 9a) over H-BEA was significantly compromised by the addition of water, with nearly no H_2 conversion, and trace products in the C_4–C_{13} range. In contrast, Co_1Ni_1/BEA maintained substantial activity (∼30% H_2 conversion) despite a reduction from its dry benchmark (∼50% H_2 conversion), remaining markedly more active than H-BEA. This confirms the critical role of metal sites in maintaining activity in the presence of water. Hydrocarbon-type selectivity (Fig. 9b) further emphasized this divergence. H-BEA yielded an orange/yellow aromatic-rich liquid and tar-like solids (Fig. 9d), indicative of condensation of aromatics which are precursors to coke formation. The bimetallic catalyst, by contrast, yielded transparent products with low aromatic content, reflecting effective hydrogenation of unsaturated
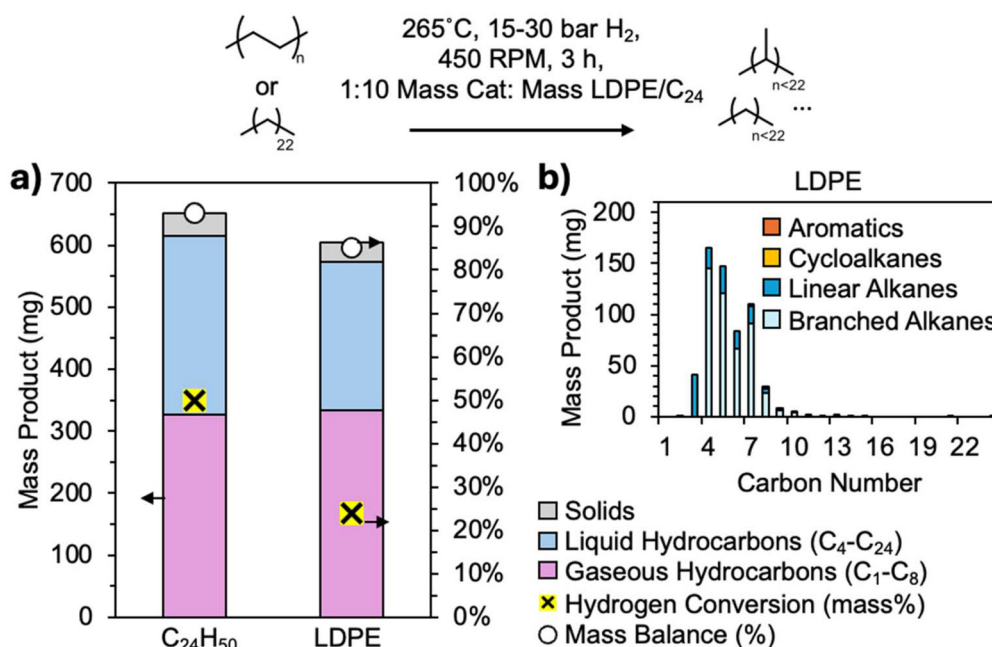
Fig. 10 (a) Product yield and phase distribution from LDPE and tetracosane hydrocracking over Co_1Ni_1/BEA at 265 °C, 20 bar H_2 (700 mg substrate, 70 mg catalyst, 3 h reaction), (b) carbon number distribution ($C_1–C_{20+}$) of products, categorized as linear alkanes (dark blue), branched alkanes (light blue), and cycloalkanes (yellow).

intermediates. BET N_2 adsorption isotherms (Fig. S3) further support this trend. Post-reaction H-BEA exhibited markedly reduced N_2 uptake under wet conditions compared to its dry counterpart, consistent with pore blockage by water-induced condensation products and coke. In contrast, Co_1Ni_1/BEA maintained higher surface area and pore accessibility than wet H-BEA, with only a modest decrease relative to its dry benchmark. This aligns with the TGA profiles (Fig. 9c), which show significantly higher coke deposition for H-BEA, with larger mass loss in the range of 300–600 °C indicating the presence of hard coke.[62] In contrast, Co_1Ni_1 /BEA formed mostly soft coke (150–350 °C), further supporting the role of metal sites in suppressing aromatic condensation. Carbon number distributions (Fig. S29a and b) highlight key differences in product profiles. H-BEA generated more $C_9–C_{13}$ aromatics, characteristic of acid-catalyzed oligomerization and aromatization. Conversely, Co_1Ni_1/BEA showed a broader, alkane-dominated profile centered on $C_5–C_8$, indicating better hydrogen activation and consumption. GC analysis of the H-BEA product showed poor mass recovery, which is likely due to the formation of heavy polyaromatic hydrocarbons (PAHs) that exceed GC detection limits or condense into non-volatile residues.[63] These undetected products also align with the observed visual tar formation and high TGA mass loss. To further validate the formation of these aromatic and polyaromatic species, ^{1}H NMR analysis of the liquid products under wet conditions confirmed pronounced aromatic and benzylic resonances for H-BEA, consistent with the presence of PAH intermediates,[64] whereas Co_1Ni_1/BEA showed predominantly aliphatic signals, confirming effective hydrogenation and sup-

pression of aromatic condensation (Fig. S30 and S31). Taken together, H-BEA deactivates rapidly under wet conditions, promoting aromatic condensation and coke formation, whereas Co_1Ni_1/BEA remains active and selective. These results highlight the importance of metal function and bimetallic design for hydrocracking in moist environments.

To extend the study beyond model compounds, LDPE hydrocracking was performed using Co_1Ni_1/BEA at 265 °C and 20 bar H_2 with a 1 : 10 catalyst-to-substrate ratio. This catalyst was selected based on its optimal hydrogenolysis/β-scission balance observed in model compound studies. Catalytic activity (Fig. 10a) showed ~24% hydrogen conversion, significantly lower than for tetracosane (~50% hydrogen conversion). This decline is attributed to LDPE's high molecular weight, semi-crystalline structure, and low hydrogen solubility (~10^{-3} g_{H_2} g_{LDPE}^{-1} at 90 °C, 8 atm).[65] Additionally, magnetic stirring provides only limited mixing and gas–liquid–solid mass transfer.[66,67] Despite sufficient H_2 supply (~60 mg), local hydrogen availability likely remains restricted, highlighting the need for improved mixing and reactor design in future applications. Product selectivity (Fig. 10b) remained favorable, with high $C_3–C_7$ alkane selectivity and minimal CH_4, closely resembling trends from tetracosane hydrocracking.

These results demonstrate that Co–Ni/BEA enables selective LDPE hydrocracking for model systems with varying molecular weights to produce liquid and gas range alkanes. The reusability of Co_1Ni_1/BEA across three consecutive tetracosane hydrocracking cycles (Fig. S32 and S33 and Table S10) further confirmed its durability, maintaining stable gaseous yields and suppressed methane formation despite moderate de-

activation attributed to metal agglomeration and/or pore blockage. While the liquid-range products have a large market for fuels, the capacity to convert PE into light hydrocarbons (propane, isobutane) offers the opportunity to dehydrogenate the alkane to produce monomers (propylene, isobutene), enabling a circular economy.

4. Conclusions

This study established bimetallic Co–Ni/BEA catalysts as stable, earth-abundant alternatives to noble metals for hydrocracking long-chain hydrocarbons and polyethylene. Tuning the Co/Ni ratio enabled increased hydrogen activation, suppressed methane formation, and minimized coke formation, even in the presence of water, which deactivated the unmodified zeolite H-BEA. Notably, partially replacing cobalt with nickel reduces reliance on cobalt, without compromising performance. The optimized 1 : 1 Co/Ni composition demonstrated superior activity and selectivity, owing to synergistic effects including improved dispersion and hydrogen surface coverage supported by catalyst characterization and reactivity studies. TEM and CO Pulse Chemisorption both suggest that the Co–Ni catalysts have increased dispersion as indicated by their lower average particle diameter and higher CO uptake. BET and TGA measurements suggest that the Co–Ni/BEA catalyst has improved surface area and resilience to coke formation in the pores. Structural characterization including XRD and XPS suggest that the crystal structure and oxidation states of Co and Ni are not significantly impacted upon co-impregnation, suggesting that the synergistic effect is not purely electronic, but rather driven by proximal Ni and Co domains which promote both polymer and hydrogen activation. Studies of the impact of temperature and hydrogen pressure show that addition of Ni to Co prevents methane formation across a broad temperature and pressure range, suggesting that the Ni promotes hydrogen activation to maintain an ideal balance of surface hydrogen and adsorbed polyethylene to cleave non-terminal carbon–carbon bonds and prevent over-hydrogenolysis to methane. The successful application to LDPE, and the facile catalyst synthesis method, underscored the real-world relevance of this catalyst system. Overall, this work advanced the development of scalable, water-tolerant, and cost-effective catalyst platforms for plastic waste valorization under realistic conditions and opens doors to future investigations into the synthesis of uniform and well-dispersed bimetallic nanoparticles and the impact of internal pore confinement on activity and selectivity.

Author contributions

Mahdokht Soltani: performed the experiments, analyzed the data, writing – original draft, writing – review & editing; Julia N. Hancock: assisted with method development and characterization, writing – review & editing; Zeno R. Ramadhan: per-

formed TEM analysis; Samuel Somerville: performed XPS analysis; Jamie Clark: performed XRD measurements; Richard Tilley: provided resources, supervised TEM and XPS work; Julie E. Rorrer: conceptualization, resources, supervision, and writing – review & editing.

Conflicts of interest

There are no conflicts of interest to report.

Data availability

All data needed to evaluate the conclusions in this paper are included in the main text and supplementary information (SI). Supplementary information: additional figures, tables, and experimental details, including catalyst characterization data, extended catalytic performance results, and supplementary discussions. See DOI: https://doi.org/10.1039/d5gc04620c.

Acknowledgements

References

1 M. Dokl, A. Copot, D. Krajnc, Y. V. Fan, A. Vujanović, K. B. Aviso, R. R. Tan, Z. Kravanja and L. Čuček, *Sustain. Prod. Consum.*, 2024, **51**, 498–518.

2 R. Tiwari, N. Azad, D. Dutta, B. R. Yadav and S. Kumar, *Sci. Total Environ.*, 2023, **881**, 163433.

3 R. Geyer, J. R. Jambeck and K. L. Law, *Sci. Adv.*, 2017, **3**, e1700782.

4 T. P. Hendrickson, B. Bose, N. Vora, T. Huntington, S. L. Nordahl, B. A. Helms and C. D. Scown, *One Earth*, 2024, 7, 520–531.

5 G. Bonifazi, G. Capobianco and S. Serranti, *Spectrochim. Acta, Part A*, 2018, **198**, 115–122.

6 S. R. Nicholson, J. E. Rorrer, A. Singh, M. O. Konev, N. A. Rorrer, A. C. Carpenter, A. J. Jacobsen, Y. Román-Leshkov and G. T. Beckham, *Annu. Rev. Chem. Biomol. Eng.*, 2022, **13**, 301–324.

7 H. Li, H. A. Aguirre-Villegas, R. D. Allen, X. Bai, C. H. Benson, G. T. Beckham, S. L. Bradshaw, J. L. Brown, R. C. Brown, V. S. Cecon, J. B. Curley, G. W. Curtzwiler, S. Dong, S. Gaddameedi, J. E. García, I. Hermans, M. S. Kim, J. Ma, L. O. Mark, M. Mavrikakis, O. O. Olafasakin, T. A. Osswald, K. G. Papanikolaou, H. Radhakrishnan, M. A. Sanchez Castillo, K. L. Sánchez-Rivera, K. N. Tumu, R. C. Van Lehn, K. L. Vorst, M. M. Wright, J. Wu, V. M. Zavala, P. Zhou and G. W. Huber, *Green Chem.*, 2022, **24**, 8899–9002.

8 Q. Hou, M. Zhen, H. Qian, Y. Nie, X. Bai, T. Xia, M. Laiq Ur Rehman, Q. Li and M. Ju, *Cell Rep. Phys. Sci.*, 2021, **2**, 100514.

9 A. Musa, E. A. Jaseer, S. Barman and N. Garcia, *Energy Fuels*, 2024, **38**, 1676–1691.

10 H. Lei, Z. Wang, S. Li and M. Zhu, *Green Chem.*, 2025, **27**, 9357–9413.

11 M. Chu, Y. Liu, X. Lou, Q. Zhang and J. Chen, *ACS Catal.*, 2022, **12**, 4659–4679.

12 S. Armenise, W. SyieLuing, J. M. Ramírez-Velásquez, F. Launay, D. Wuebben, N. Ngadi, J. Rams and M. Muñoz, *J. Anal. Appl. Pyrolysis*, 2021, **158**, 105265.

13 M. Artetxe, G. Lopez, G. Elordi, M. Amutio, J. Bilbao and M. Olazar, *Ind. Eng. Chem. Res.*, 2012, **51**, 13915–13923.

14 M. Lu, S. Wang, M. Su, Z. Weng, J. Zheng, N. K. Gupta, K. Cai, Z. Shou and Q. Ke, *Ind. Eng. Chem. Res.*, 2025, **64**, 5765–5781.

15 J. E. Rorrer, G. T. Beckham and Y. Román-Leshkov, *JACS Au*, 2021, **1**, 8–12.

16 B. C. Vance, P. A. Kots, C. Wang, J. E. Granite and D. G. Vlachos, *Appl. Catal., B*, 2023, **322**, 122138.

17 S. S. Borkar, R. Helmer, S. Panicker and M. Shetty, *ACS Sustainable Chem. Eng.*, 2023, **11**, 10142–10157.

18 G. Celik, R. M. Kennedy, R. A. Hackler, M. Ferrandon, A. Tennakoon, S. Patnaik, A. M. LaPointe, S. C. Ammal, A. Heyden, F. A. Perras, M. Pruski, S. L. Scott, K. R. Poeppelmeier, A. D. Sadow and M. Delferro, *ACS Cent. Sci.*, 2019, **5**, 1795–1803.

19 L. Chen, Y. Zhu, L. C. Meyer, L. V. Hale, T. T. Le, A. Karkamkar, J. A. Lercher, O. Y. Gutiérrez and J. Szanyi, *React. Chem. Eng.*, 2022, **7**, 844–854.

20 A. Tennakoon, X. Wu, A. L. Paterson, S. Patnaik, Y. Pei, A. M. LaPointe, S. C. Ammal, R. A. Hackler, A. Heyden, I. I. Slowing, G. W. Coates, M. Delferro, B. Peters, W. Huang, A. D. Sadow and F. A. Perras, *Nat. Catal.*, 2020, **3**, 893–901.

21 J. E. Rorrer, A. M. Ebrahim, Y. Questell-Santiago, J. Zhu, C. Troyano-Valls, A. S. Asundi, A. E. Brenner, S. R. Bare, C. J. Tassone, G. T. Beckham and Y. Román-Leshkov, *ACS Catal.*, 2022, **12**, 13969–13979.

22 C. Wang, T. Xie, P. A. Kots, B. C. Vance, K. Yu, P. Kumar, J. Fu, S. Liu, G. Tsilomelekis, E. A. Stach, W. Zheng and D. G. Vlachos, *JACS Au*, 2021, **1**, 1422–1434.

23 *Noble and Precious Metals: Properties, Nanoscale Effects and Applications*, ed. M. Singh Seehra and A. D. Bristow, IntechOpen, Erscheinungsort nicht ermittelbar, 2018.

24 S. Sun and W. Huang, *JACS Au*, 2024, **4**, 2081–2098.

25 B. C. Vance, Z. Yuliu, S. Najmi, E. Selvam, J. E. Granite, K. Yu, M. G. Ierapetritou and D. G. Vlachos, *Chem. Eng. J.*, 2024, **487**, 150468.

26 J. Z. Tan, C. W. Hullfish, Y. Zheng, B. E. Koel and M. L. Sarazen, *Appl. Catal., B*, 2023, **338**, 123028.

27 R. Cong, J. Zhan, R. Dai, H. Luo, H. Zhou, L. Xia and H. Wang, *Catal. Sci. Technol.*, 2025, **15**, 2606–2616.

28 J. Zhan, R. Dai, R. Cong, Y. Dan, H. Luo, H. Zhou, L. Xia, S. Zhang and H. Wang, *Green Chem.*, 2025, **27**, 3398–3412.

29 E. Rytter, T. H. Skagseth, S. Eri and A. O. Sjåstad, *Ind. Eng. Chem. Res.*, 2010, **49**, 4140–4148.

30 F. J. Vela, R. Palos, J. Bilbao, J. M. Arandes and A. Gutiérrez, *Catalysts*, 2024, **14**, 203.

31 M. Sun, L. Zhu, W. Liu, X. Zhao, Y. Zhang, H. Luo, G. Miao, S. Li, S. Yin and L. Kong, *Sustainable Energy Fuels*, 2022, **6**, 271–275.

32 A. K. Aboul-Gheit, S. M. Aboul-Fotouh and N. A. K. Aboul-Gheit, *Appl. Catal., A*, 2005, **292**, 144–153.

33 W. Yin, R. H. Venderbosch, S. He, M. V. Bykova, S. A. Khromova, V. A. Yakovlev and H. J. Heeres, *Biomass Convers. Biorefin.*, 2017, **7**, 361–376.

34 J. Wildschut, F. H. Mahfud, R. H. Venderbosch and H. J. Heeres, *Ind. Eng. Chem. Res.*, 2009, **48**, 10324–10334.

35 S. Wang, Q. Yin, J. Guo, B. Ru and L. Zhu, *Fuel*, 2013, **108**, 597–603.

36 C. Hernández Mejía, J. E. S. Van Der Hoeven, P. E. De Jongh and K. P. De Jong, *ACS Catal.*, 2020, **10**, 7343–7354.

37 P. Van Helden, F. Prinsloo, J.-A. Van Den Berg, B. Xaba, W. Erasmus, M. Claeys and J. Van De Loosdrecht, *Catal. Today*, 2020, **342**, 88–98.

38 J. Weitkamp, *ChemCatChem*, 2012, **4**, 292–306.

39 W.-T. Lee, A. Van Muyden, F. D. Bobbink, M. D. Mensi, J. R. Carullo and P. J. Dyson, *Nat. Commun.*, 2022, **13**, 4850.

40 D. Romero, M. Rigutto and E. J. M. Hensen, *Fuel*, 2024, **358**, 130264.

41 J. A. Sun, E. Selvam, A. Bregvadze, W. Zheng and D. G. Vlachos, *Green Chem.*, 2025, **27**, 3905–3915.

42 D. E. Resasco, S. P. Crossley, B. Wang and J. L. White, *Catal. Rev.*, 2021, **63**, 302–362.

43 T. Kwon, B. Ahn, K. H. Kang, W. Won and I. Ro, *Nat. Commun.*, 2024, **15**, 10239.

44 A. Singh, N. A. Rorrer, S. R. Nicholson, E. Erickson, J. S. DesVeaux, A. F. T. Avelino, P. Lamers, A. Bhatt, Y. Zhang, G. Avery, L. Tao, A. R. Pickford, A. C. Carpenter, J. E. McGeehan and G. T. Beckham, *Joule*, 2021, **5**, 2479–2503.

45 M. A. Camblor, A. Corma, A. Martínez, V. Martínez-Soria and S. Valencia, *J. Catal.*, 1998, **179**, 537–547.

46 A. E. Brenner, G. Drake, G. T. Beckham and Y. Román-Leshkov, JACS Au, 2025, **5**(8), 4123–4132.

47 A. Bin Jumah, V. Anbumuthu, A. A. Tedstone and A. A. Garforth, *Ind. Eng. Chem. Res.*, 2019, **58**, 20601–20609.

48 M. N. Gebresillase, R. Q. Raguindin, H. Kim and J. G. Seo, *Catalysts*, 2020, **10**, 1354.

49 Y. Yao and D. W. Goodman, *J. Mol. Catal. A: Chem.*, 2014, **383–384**, 239–242.

50 C. Bernardon, M. Ben Osman, G. Laugel, B. Louis and P. Pale, *C. R. Chim.*, 2016, **20**, 20–29.

51 N. Nunes, A. P. Carvalho, R. Elvas-Leitão, F. Martins, A. Fernandes, J. Rocha and A. Martins, *Catalysts*, 2022, **12**, 1064.

52 S.-R. Chung, K.-W. Wang, S.-R. Sheen, C.-T. Yeh and T.-P. Perng, *Electrochem. Solid-State Lett.*, 2007, **10**, A155–A158.

53 Y. Gao, Z. J. Zheng, M. Q. Zeng, C. P. Luo and M. Zhu, *J. Mater. Res.*, 2008, **23**, 1343–1349.

54 R. Zou, G. A. Bramley, S. Xu, S. Chansai, M. Panchal, H. Chen, Y. Zhou, P. Gao, G. Hou, S. M. Holmes, C. Hardacre, Y. Jiao, A. J. Logsdail and X. Fan, *Catal. Sci. Technol.*, 2024, **14**, 164–173.

55 D. Perilli, V. Chesnyak, A. Ugolotti, M. Panighel, S. Vigneri, F. Armillotta, P. Naderasli, M. Stredansky, M. Schied, P. Lacovig, S. Lizzit, C. Cepek, G. Comelli, H. Brune, C. Africh and C. Di Valentin, *Angew. Chem., Int. Ed.*, 2025, **64**, e202421757.

56 B. Todic, W. Ma, G. Jacobs, N. Nikacevic, B. H. Davis and D. B. Bukur, *Int. J. Chem. Kinet.*, 2017, **49**, 859–874.

57 Y. Bai, D. Liu, L. Zhao, J. Gao, C. Xu, H. Pang and X. Gao, *Ind. Eng. Chem. Res.*, 2022, **61**, 15842–15855.

58 M. Fattahi, R. M. Behbahani and T. Hamoule, *Fuel*, 2016, **181**, 248–258.

59 T. H. Lim, S. J. Cho, H. S. Yang, M. H. Engelhard and D. H. Kim, *Appl. Catal., A*, 2015, **505**, 62–69.

60 Y. Hou, S. Nagamatsu, K. Asakura, A. Fukuoka and H. Kobayashi, *Commun. Chem.*, 2018, **1**, 41.

61 L. Wang, S. He, L. Wang, Y. Lei, X. Meng and F.-S. Xiao, *ACS Catal.*, 2019, **9**, 11335–11340.

62 R. Ahmed, C. M. Sinnathamb and D. Subbarao, *J. Appl. Sci.*, 2011, **11**, 1225–1230.

63 Y. Lv, X. Li, T. T. Xu, T. T. Cheng, X. Yang, J. M. Chen, Y. Iinuma and H. Herrmann, *Atmos. Chem. Phys.*, 2016, **16**, 2971–2983.

64 F. Zhang, M. Zeng, R. D. Yappert, J. Sun, Y.-H. Lee, A. M. LaPointe, B. Peters, M. M. Abu-Omar and S. L. Scott, *Science*, 2020, **370**, 437–441.

65 J. Sun, H. Wang, M. Chen, J. Ye, B. Jiang, J. Wang, Y. Yang and C. Ren, *J. Appl. Polym. Sci.*, 2017, **134**, 44507.

66 S. D. Jaydev, A. J. Martín, D. Garcia, K. Chikri and J. Pérez-Ramírez, *Nat. Chem. Eng.*, 2024, **1**, 565–575.

67 M. Soltani and J. E. Rorrer, *Nat. Chem. Eng.*, 2024, **1**, 557–558.